

Issues in the Quantitation of Reoriented Cardiac PET Images

William G. Kuhle, Gerold Porenta, Sun-Chen Huang, Michael E. Phelps, and Heinrich R. Schelbert

Division of Nuclear Medicine and Biophysics, Department of Radiological Sciences, UCLA School of Medicine, University of California, Los Angeles, California and Laboratories of Nuclear Medicine and Biomedical and Environmental Sciences, University of California, Los Angeles, California

Reorientation of transaxial cardiac PET images into short-axis images has been shown by other investigators to improve visual identifiability of defects in myocardial tracer uptake. However, quantification of physiologic processes from such reoriented images may be complicated by errors introduced during the reorientation process. Therefore, a quantitative characterization of these errors is necessary. An annular phantom of human cardiac dimensions was imaged in a 15-plane positron emission tomograph at six angles (0°, 5°, 25°, 45°, 65°, 85°) and at two different axial sampling densities. In addition, two different reorientation interpolators were employed, one using three-dimensional linear interpolation and the other using a "hybrid" interpolation algorithm. Distortion of linear distances was variable but was minimized with denser axial sampling and the use of hybrid interpolation. Circumferential profile analysis, corrected for inhomogeneities in reoriented image spatial resolution, revealed a maximal loss of region of interest counts at 65° of at least 14.4%. Reorientation errors were minimized by use of dense axial sampling, low angles of reorientation and use of the hybrid interpolation algorithm.

J Nucl Med 1992; 33:1235-1242

Standard cardiac positron emission tomography (PET) provides transaxial images of the heart. Because the long-axis of the left ventricle is generally not aligned with the axis of the scanner, the transaxial planes pass obliquely through the left ventricular myocardium. Due to interpatient variability in the heart's orientation, the display of the heart in transaxial myocardial images may vary considerably, which complicates visual interpretation of the images. The obliquity of the transaxial sections results in apparent but artifactual regional differences in myocardial wall thickness and, consequently, in count recovery which creates artificial inhomogeneities in the imaged tissue radionuclide concentrations. Senda et al. (1) observed for example that the obliquity present in transaxial images

may mask myocardial perfusion defects. The same obliquity of images also precludes the generation of polar maps of the three-dimensional distribution of functional processes throughout the left ventricular myocardium (2).

Short-axis sections would reduce the effects of interpatient variability in left ventricular orientation, reduce the effects of obliquity, facilitate precise location of quantitated parameters and allow generation of polar maps. Reorientation of transaxially-acquired cardiac images into standard short-axis and long-axis views has therefore become routine in SPECT imaging (2-5). Other investigators (1,6-8) have reported preliminary observations in visual and quantitative terms for reoriented cardiac PET images. Reorientation of the heart into short- and long-axis views, for example, has been found to improve the sensitivity and specificity of identifying visually regional perfusion defects in the left ventricular myocardium (1).

Quantification of functional processes from reoriented images requires characterization of the errors introduced by the reorientation. Determinants of reorientation errors include: (a) the density of the spatial sampling, (b) the angle of reorientation (i.e., between the long-axis of the left ventricle and the axis of the tomograph) and (c) the type of interpolation algorithm used. Reorientation involves multidimensional interpolation of the original volume of data. Because interpolation is equivalent to a linear, low-pass digital filtering operation (9,10), modification of the reoriented images from the original is inevitable.

The purpose of this study was to characterize quantitatively possible deleterious effects of reorientation on tissue radioactivity concentrations and image geometry. Radioactivity concentrations and geometric distortion in reoriented phantom images were examined and quantified with a cardiac phantom for: (a) variations in the density of axial sampling, (b) different angles of reorientation and (c) two different interpolation algorithms.

MATERIALS AND METHODS

Cardiac Phantom

A lucite cardiac phantom (Fig. 1) consisting of three concentric cylindrical chambers was imaged. The middle chamber of the phantom represented the left ventricular myocardium with a wall

Received Apr. 4, 1991; revision accepted Jan. 8, 1992.

For reprints contact: Heinrich R. Schelbert, MD, Division of Nuclear Medicine and Biophysics, UCLA School of Medicine, Los Angeles, CA 90024-1721.

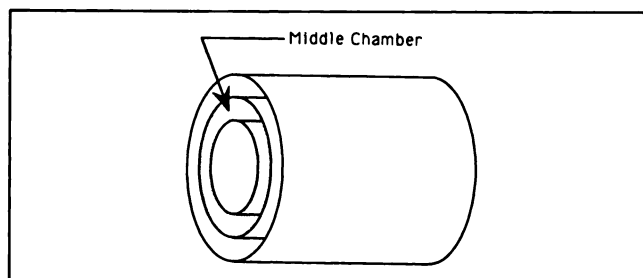


FIGURE 1. The cylindrical cardiac phantom used in the experiments has three chambers. The middle chamber, which carried the radioactive tracer, is 10 mm thick. The inner and outer chambers were filled with water. A long plastic screw placed in the middle chamber created an imaging defect.

thickness of 10 mm. The diameter of the inner chamber was 55 mm and the outer diameter of the outer chamber was 100 mm. The phantom's length was 100 mm. The volume of its middle chamber was measured to be 215 ml. A small imaging defect was created in the middle chamber by insertion of a long, 5-mm diameter plastic screw oriented parallel to the axis of the cylinder. The phantom was placed in the tomograph so that the defect appeared in the phantom's anterior wall. All three chambers were initially filled with water.

PET

The phantom was mounted on the bed of a Siemens 931-08 tomograph (simultaneous acquisition of 15 planes; 128×128 pixels per plane; 1.56 mm^2 per pixel; 6.75 mm plane separation; axial FWHM of 7 mm) with the axis of the phantom initially aligned with the axis of the tomograph. The phantom was imaged at six angles of offset (0° , 5° , 25° , 45° , 65° , 85°) in the tomograph's azimuthal plane and at two bed positions 3 mm apart, thus giving a total of twelve different geometric configurations imaged. The two bed positions (subsequently referred to as the "upper" and "lower" bed positions, respectively) allowed for interleaving of planes, thus doubling the axial sampling and halving the ratio of plane separation to pixel size. Imaging of the phantom with offset angles in the azimuthal plane only (the phantom's angle of elevation set to 0°) was sufficient because the tomograph's point spread function (PSF) is circularly symmetric in the transaxial plane.

The twelve different geometric configurations required twelve transmission and emission scans. Transmission images were obtained when the phantom's middle chamber contained only water. Emission scanning was done in the tomograph's non-wobbled mode after 4.1 mCi ^{18}F FDG had been introduced into the phantom's middle chamber. All emission images were acquired with at least 2×10^6 counts per plane and all were reconstructed using a 0.30 cycles/pixel Shepp-Logan filter giving a final transaxial FWHM of 10.5 mm. Figure 2 illustrates the frame imaged with a 65° angular offset from the scanner's axis. At each angle except 0° , the frames from the upper and lower bed positions were interleaved, thus forming a third frame consisting of 30 planes with an interplane spacing of 3.375 mm.

Image Reorientation

Two different three-dimensional interpolators were used to reorient the images. The first interpolator employed conventional three-dimensional linear interpolation, while the second interpolator was a "hybrid" approach consisting of a two-dimensional

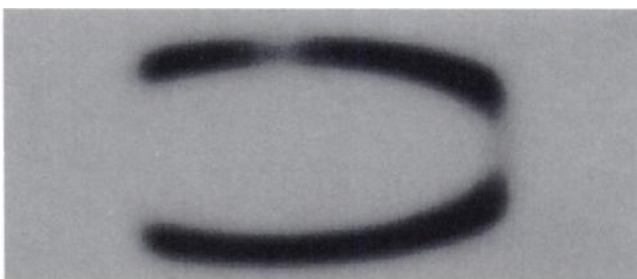


FIGURE 2. This plane was acquired from the phantom which was offset 65° from the axis of the scanner. Note the defect in the anterior wall.

linear interpolator inplane and a one-dimensional cubic convolution interpolator across planes in the axial direction. This hybrid approach was taken because the inplane grid of 128×128 pixels was thought to be of fine enough spatial sampling to warrant linear interpolation, while the axial sampling of 6.75 mm in the noninterleaved case was coarse enough to require a more sophisticated interpolation algorithm.

The cubic convolution interpolation algorithm employed in this study had previously been derived and characterized by others (11,12). The order of accuracy of cubic convolution interpolation is between that of linear interpolation and cubic spline interpolation. The one-dimensional kernel in the cubic convolution interpolator is a piecewise third-order (cubic) polynomial defined on the intervals $(-2,-1)$, $(-1,0)$, $(0,1)$, and $(1,2)$; elsewhere the kernel is zero. In a one-dimensional interpolation using cubic convolution, four points are needed to calculate one interpolated point. This renders cubic convolution interpolation computationally more efficient than cubic spline interpolation yet not as computationally efficient as linear interpolation, which, in one-dimension, requires only two data points to calculate one interpolated value (11,12).

All image processing and analysis were performed on a Macintosh II computer (16 MHz clock, MC68020 processor with floating point coprocessor, 8 MB RAM). The custom reorientation software was written specifically for this system. Prior to image reorientation, all planes of all frames were scaled into the range 0 to 255 (8 bits per pixel). Except for the frames acquired at the 0° position, all frames were then reoriented back to 0° azimuth. With the plane spacing of the reoriented images always set to 6.75 mm, 15 reoriented planes were produced from each offset frame.

Image Analysis

Following reorientation, the resliced planes were matched to the planes of the control frame at 0° , and the matched pairs of images were analyzed for differences in geometric distortion and image counts. Geometric distortion was assessed by determining how well reorientation preserved the linear distance between two points of known separation. In cardiac studies, the thickness of the left ventricular myocardium is a parameter of clinical interest which motivated the use of the phantom's uniform wall thickness to gauge any distorting effects due to reorientation. The wall thickness at each of 60 sectors of the reoriented phantoms was estimated and compared to those obtained from the phantom in the control position (at 0°).

The relatively low spatial resolution of current PET scanners affects the estimation of the linear distance between two points

when that distance is on the order of the FWHM. Therefore, the effects of reorientation on spatial resolution cannot be ignored and will be characterized first. It will be shown that for tomographs in which the point-spread function is not spherically symmetric, the spatial resolution in a reoriented PET image varies according to the direction a line travels in as it passes through any point in the image. This fact precludes a direct assessment of distortion in reoriented images by subtraction on a pixel-by-pixel basis of the reoriented image from the control image.

Spatial resolution in PET imaging is usually described in terms of the FWHM of the scanner's intrinsic three-dimensional PSF, together with the effective loss in transaxial resolution by use of image reconstruction filters other than ramp filter. In order to estimate the spatial resolution of the reoriented images, first consider the commonly-used Gaussian approximation to the scanner's three-dimensional PSF (13):

$$\text{PSF} = \exp(-x^2/2\sigma_x^2 - y^2/2\sigma_y^2 - z^2/2\sigma_z^2), \quad \text{Eq. 1}$$

where $\sigma_x = \text{FWHM}_x/2.355$, $\sigma_y = \text{FWHM}_y/2.355$ and $\sigma_z = \text{FWHM}_z/2.355$.

The x and y coordinates lie in the scanner's transaxial plane, while the z coordinate lies along the scanner's axis. Assume that $\text{FWHM}_x = \text{FWHM}_y \neq \text{FWHM}_z$, as is the case for the scanner used in this study. An isocontour of the PSF then defines an ellipsoid in three-space, with the principal axes of the ellipsoid aligned with the scanner's (x,y,z) rectangular coordinate system. During image reorientation, this ellipsoid is, in general, not cut along one of its principal axes but in an oblique fashion. The intersection of the ellipsoid with a plane of reorientation (a plane that passes through the origin of the (x,y,z) system) defines an ellipse. It is this ellipse of intersection that determines the spatial resolution of the reoriented images. That is, the distance from the center of the ellipse to its edge in a particular direction gives the spatial resolution of the reoriented image in that direction (see Appendix for details).

Once the effective spatial resolution $\text{FWHM}_{\text{eff},\theta}$ in the direction specified by the angle θ has been determined, it is possible to estimate the wall thickness of the phantom in that same direction

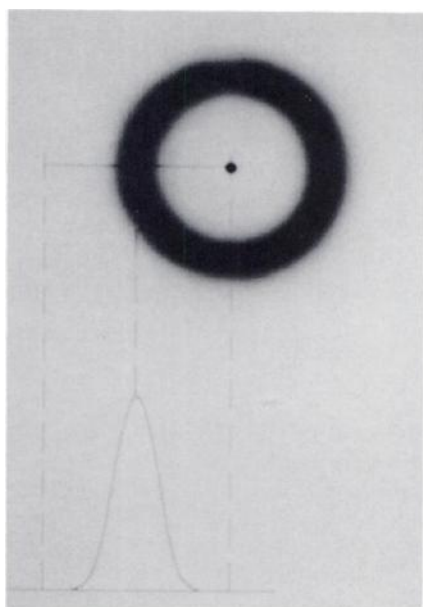


FIGURE 3. A short-axis image of the phantom with a superimposed ray. The imaged activity distribution is shown plotted along a radial coordinate. This distribution or "profile" has a functional form given by Equation 2. From this profile, the wall thickness of the phantom's middle chamber can be estimated.

as follows. Suppose that the imaged phantom's short-axis view appears as shown in Figure 3. A radial profile through the imaged phantom wall can be approximated (13) by the following equation:

$$\text{Profile}(r) = (C_m/2) \left[\text{erf}\left(\frac{r-R}{\sigma_{\text{eff},\theta}\sqrt{2}}\right) - \text{erf}\left(\frac{r-R-d}{\sigma_{\text{eff},\theta}\sqrt{2}}\right) + \text{erf}\left(\frac{r+R+d}{\sigma_{\text{eff},\theta}\sqrt{2}}\right) - \text{erf}\left(\frac{r+R}{\sigma_{\text{eff},\theta}\sqrt{2}}\right) \right], \quad \text{Eq. 2}$$

where C_m is the true activity in the phantom wall, R is the radius of the inner chamber of the phantom, d is the wall thickness of the phantom and $\text{erf}(\cdot)$ is the error function. By using nonlinear parameter estimation techniques [e.g., the Levenberg-Marquardt method (14)], this equation can be fit to the measured profile for the parameters C_m , R and d . In this study, the resulting estimate of the wall thickness d from the reoriented phantom, averaged over the sixty sectors, was compared to the average estimate of the wall thickness obtained from the control phantom, and differences in the average wall thicknesses were analyzed for statistical significance using the single-sample t-test. Probability values of less than 0.05 were considered statistically significant.

Image counts were assessed by circumferential profile analysis. Although the circumferential activity profile consisted of 60 equally-spaced sectors, only every third sector of the contour was used in the analysis, ensuring that the measurements from adjacent sectors were statistically independent. Figure 4 illustrates a control plane and a 60-sector contour used. Sector 1 is located at the 9 o'clock position, and the sector numbers increase in the clockwise direction.

As indicated above, the spatial resolution in reoriented images can vary with the direction of travel within the image itself, and hence, from sector to sector. Thus, the effect of partial volume on activity in the circumferential sectors of the reoriented images varies around the circumference. In contrast, the effect of partial volume on activity in the sectors of the control images is constant because the spatial resolution in the transaxial plane is uniform. Since the partial volume effects between the two sets of images will therefore not offset each other, the reoriented circumferential activity profiles cannot be directly compared with those of the control. In order to adequately correct for this situation, sector activity in the control and reoriented images were both corrected for their respective partial volume effects. The partial volume corrections for both the control and reoriented images were made

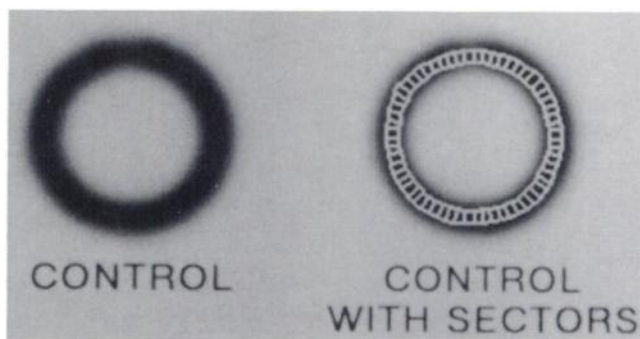


FIGURE 4. Images obtained in the control (0°) position. The image on the right has superimposed upon it the 60 sectors used in the quantitative analysis of the reoriented images.

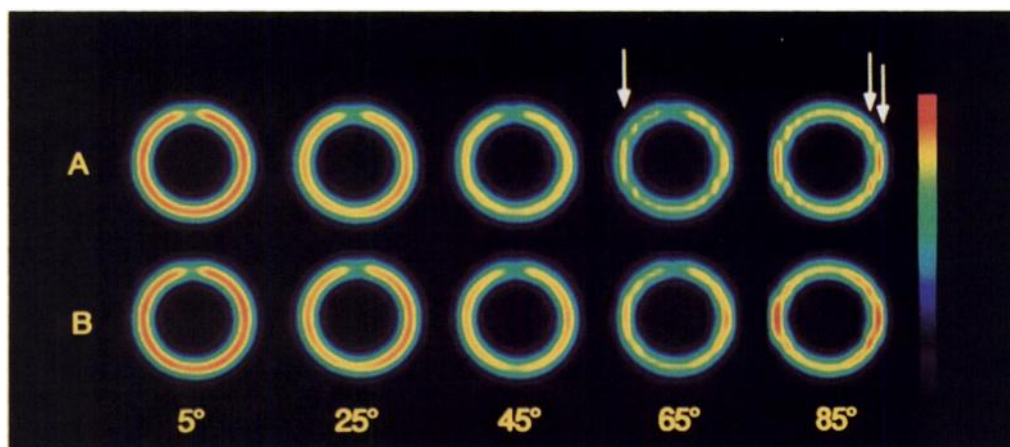


FIGURE 5. These are reoriented planes with the angles of reorientation indicated. Both upper and lower panels were derived from noninterleaved frames (15 planes per frame). (A) Each of these images was produced by the three-dimensional linear interpolation algorithm. Vertical densities are visible at reorientation angles of 65° and 85° (see arrows). Artifacts from inhomogeneities in spatial resolution are most easily seen in the 85° image in its lateral walls. The lateral walls appear more intense than the anterior and posterior walls because the spatial resolution in the lateral walls is higher than that of the anterior and posterior walls. (B) Each of these images was produced by the three-dimensional hybrid interpolation algorithm. Vertical densities are not as prominent. Artifacts from inhomogeneities in spatial resolution are also seen, especially in the 85° image.

using the phantom's known wall thickness of 10 mm, the known contour width around the circumference, and $\text{FWHM}_{\text{eff},s}$ (13). Once corrected in this way, the reoriented and control sector activity data were then analyzed for statistically significant differences using two-sample matched t-tests.

RESULTS

Visual Analysis of Reoriented Images

Undersampling Artifacts. The most evident artifacts in the reoriented phantom images are vertically-oriented linear "densities" in the lateral walls of the phantom (see arrows in Fig. 5). The presence of these artifacts decreases with a higher density of axial sampling (not shown here), lower angles of reorientation and the use of hybrid rather than linear interpolation.

Activity Inhomogeneities. Another artifact seen in Figure 5 is the apparent inhomogeneity of the circumferential activity in the reoriented phantom images caused by the nonuniform spatial resolution of the reoriented images. For example, in the 85° reoriented phantom images, there is apparently less activity near sectors 15 and 45 relative to the areas near sectors 1 and 30.

Quantitative Analysis: Noninterleaved Case

Because a 45° rotation approximates the rotation angle required for reorienting human cardiac PET images, the results from 45° reorientation are emphasized over the other angles of rotation.

Reoriented Circumferential Profiles. Figure 6A shows circumferential activity profiles from a control plane and

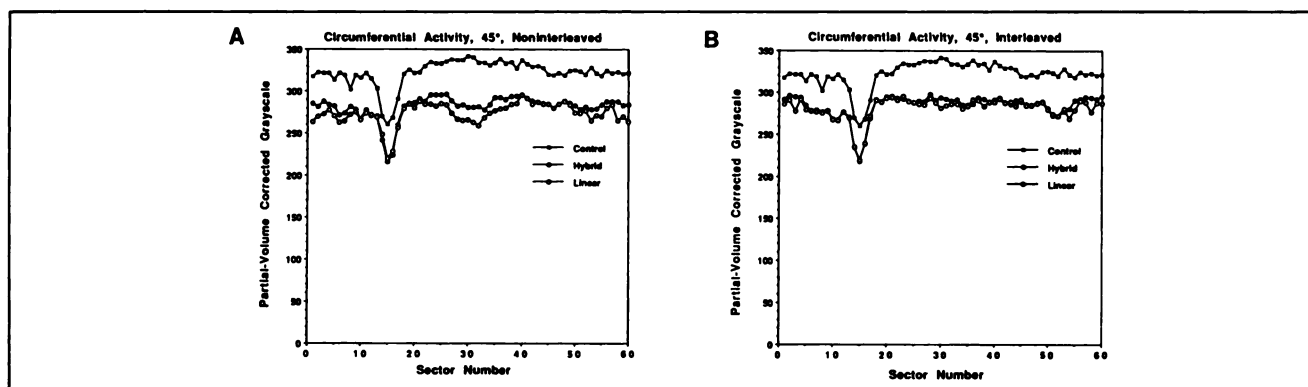


FIGURE 6. Circumferential activity profiles obtained from a control image and from 45° reoriented images using the linear and hybrid interpolators. The imaging defect is near sector 15. All profiles are corrected for partial volume effects. Note the constant loss in activity of the reoriented profiles from the control profile. (A) Images were reconstructed from noninterleaved frames. The hybrid interpolator performs better than the linear interpolator near sectors 1 and 30. (B) Images were reconstructed from interleaved frames. Note that the linear interpolator performs better near sectors 1 and 30 in this interleaved case compared to the noninterleaved case. Also, the performance of the hybrid and linear interpolators converge to each other.

TABLE 1
The Mean Percent Error in Circumferential Activity as a Function of Reorientation Angle and Type of Interpolator

Angle	Noninterleaved		Interleaved	
	%Linear error	%Hybrid error	%Linear error	%Hybrid error
5°	0.1	0.3	0.2	0.2
25°	-5.8	-4.8	-4.3	-4.3
45°	-14.9	-12.5	-12.9	-12.1
65°	-19.3	-15.9	-15.5	-14.4
85°	-17.2	-13.3	-12.5	-11.2

TABLE 2
The Mean Percent Error in Wall Thickness as a Function of Reorientation Angle and Type of Interpolator

Angle	Noninterleaved		Interleaved	
	%Linear error	%Hybrid error	%Linear error	%Hybrid error
5°	0.1	0.5	0.0	0.2
25°	3.8	3.1	2.6	2.0
45°	7.9	4.7	3.9	3.7
65°	9.2	5.8	3.5	2.5
85°	10.9	6.0	2.5	2.0

from a corresponding 45° reoriented plane based on the linear and hybrid interpolators. The vertical axis is not in absolute units but in 8-bit grayscale units (0–255) that have been corrected for partial volume effects. This correction can boost the sector activity above 255. The simulated defect is located near sector 15. Note that the circumferential profiles of the control and reoriented images are similar in shape, but there is a consistent loss of activity in the reoriented profiles. Table 1 gives the average percent errors in the reoriented circumferential activity profiles relative to the control profiles. Note that the error of the hybrid interpolator is less than that of the linear interpolator at all angles of reorientation except at 5°.

Image Distortion. Figure 7A plots the circumferential thickness profiles from a control plane and from a corresponding 45° reoriented plane. Examination of these profiles reveals that the wall thicknesses derived from the reoriented phantoms appear to be greater than those of the control. The percent errors in wall thickness versus reorientation angle are given in Table 2.

Quantitative Findings: Interleaved Case

The results of the interleaved analysis generally parallel those of the noninterleaved analysis. However, because interleaving doubles the spatial sampling in the axial di-

rection, it is expected that the errors associated with the reoriented ROI activity and wall thicknesses will decrease.

Circumferential Activity. Figure 6B plots the circumferential activity profile of a control plane against those of corresponding planes from the interleaved (30 planes), 45° reoriented phantoms. On average, though, neither interpolator markedly improves its performance over the noninterleaved case (Table 1). Table 1 also shows a convergence in performance of the two interpolators with increased axial sampling. This behavior is expected whenever the density of the spatial samples increases (11).

Image Distortion. The character and amount of distortion in the interleaved, reoriented images is given in Table 2 and Figure 7B. As in the noninterleaved case, there is an overestimation of the wall thickness. Table 2 shows that the reoriented images derived from interleaved image sets overestimate wall thickness less, especially at larger angles of reorientation, compared to reoriented noninterleaved image sets.

Finally, it is interesting to note that from Table 1 the percent errors in the average circumferential activity obtained with the *noninterleaved hybrid* interpolator are nearly the same as those seen with the *interleaved linear* interpolator. This suggests that improved interpolation in the axial direction is effectively equivalent to an increase in the density of the axial sampling.

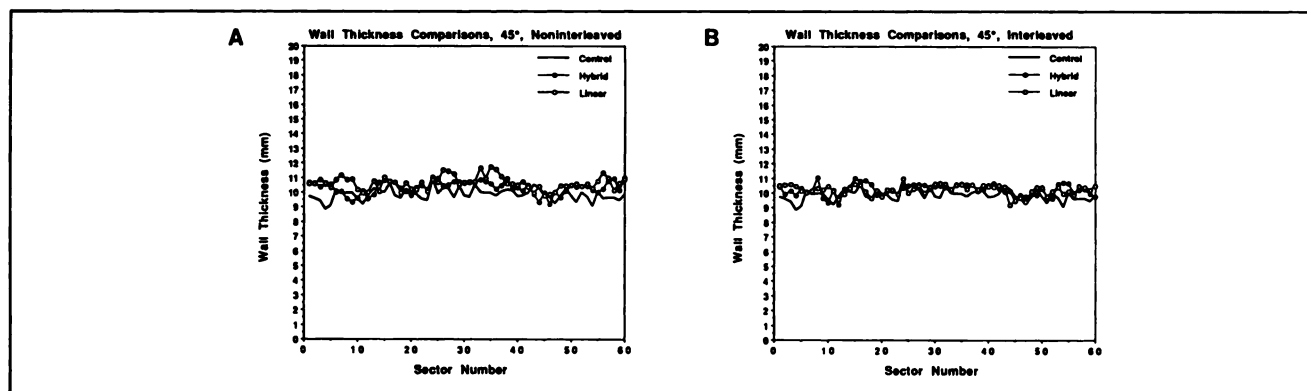


FIGURE 7. Circumferential wall thickness profiles of the control image and the 45° reoriented images. (A) The noninterleaved case shows that there is more variability in the wall thickness estimates near sectors 1 and 30, especially with the linear interpolator. (B) The interleaved case shows that the variability in the wall thickness estimates has decreased and that there is convergence of estimation performance in the two interpolators.

DISCUSSION

This study has identified effects of reorientation of cardiac PET images on the recovery of regional radioactivity concentrations. Reorientation increased the spatial distortion as measured by changes in estimated wall thickness and, more importantly, caused a net loss in tissue activity in the reoriented images, independent of partial volume effects. These effects are important for quantitative analysis of reoriented cardiac PET images. The observed reorientation errors can be understood by examining the process of reorientation itself.

Reorientation is mathematically equivalent to a three-dimensional convolution of the original discrete activity distribution with a continuous "low-pass" interpolation (or reconstruction) kernel, followed by a resampling of that continuous convolution product onto the reoriented coordinate system (9,10). If the original three-dimensional discrete activity distribution has relatively high spatial frequencies (that is, significant spectra at or near one-half of the sampling frequency in any or all of the three coordinate directions), those high spatial frequencies will be attenuated by the low-pass interpolation kernel, resulting in a smoothed, reoriented activity distribution.

In this study, the three-dimensional discrete activity distribution was derived from a three-dimensional sampling by the PET scanner of a thin-walled cardiac phantom containing ^{18}F activity. The axial sampling of the PET scanner is imperfect, especially when the phantom was tilted at the higher angles of 65° and 85° , and failed to satisfy the criteria stated in the Nyquist sampling theorem (9), thus resulting in axially-sampled data that were corrupted by aliasing. That this is true is evidenced by the vertical densities in the lateral walls of the phantom reoriented at angles of 65° and 85° (Fig. 5). These aliasing artifacts, caused by undersampling, cannot be entirely eliminated even if a perfect interpolation algorithm is used. In contrast, the sampled data in the transaxial planes are relatively well-sampled with little resultant aliasing along the transaxial coordinates. Aliasing along the axial direction results in high spatial frequencies in the three-dimensional discrete activity distribution, and thus axial activity may undergo significant smoothing when reoriented as described above. This smoothed distribution results in smearing the activity over volumes that are larger than the activity's volume in the original distribution. If similar regions of interest (ROIs) are applied to both the original and the reoriented distributions, the ROIs of the latter will have less activity than those of the former. This phenomenon of ROI activity loss was seen in the reoriented images. If the original distribution is large and smooth (i.e., the spectral content of the distribution is much less than one-half of the spatial sampling frequencies), ROI activities of the original and reoriented distributions will match each other.

Activity loss was observed to vary according to the angle of reorientation. This can be explained by understanding

that tilting the phantom in the scanner causes different activity geometries to be presented to the scanner's three-dimensional sampler. This in turn implies that the spectral content of the activity distribution along each of the scanner's three orthogonal coordinates changes with each change in phantom orientation. Thus, the degree of spectral attenuation of the distribution by the interpolation kernel will also vary when reorientation is done.

This conceptual framework of reorientation also helps to explain the larger wall thicknesses measured from the reoriented images. The profile-fitting approach used to estimate wall thickness is of course sensitive to the shape of the profile being fitted. Since the reoriented distribution will generally have wider, smoother profiles than those of the original distribution, the fitting algorithm in view of the observed data will provide wider estimates of the wall thickness.

Strategies for minimizing these errors must incorporate: (a) axial sample density, (b) the angle of reorientation and (c) the type of interpolation algorithm used to reorient the images.

Axial Sampling Density. The inplane spatial sampling in PET is typically better than axial sampling. The ratio of axial plane separation to inplane pixel size can be as large as six or more, indicating that poor axial sampling is a limiting factor when reorienting. To improve axial sampling in PET, Senda et al. (5) used an "interpolating scan" approach, in which the subject was imaged at two different axial positions. The resulting sets of images were interleaved, thus improving the axial sampling by a factor of two. The interleaved set was then reoriented and the resulting images were found to have fewer visual artifacts.

This study showed that increased axial sampling decreases the errors of reorientation. While not unexpected, other factors argue against the use of interpolating scans. The approach requires twice as much storage and processing, and either twice as much imaging time or one-half as many counts per plane (if the acquisition times for each bed position are halved). There are, however, new multiplane PET devices (15,16) that provide very good sampling density, both inplane and in the axial direction so that sampling density may become less of an issue in the near future. However, even when the axial sampling density was increased to one plane every 3.4 mm, hybrid interpolation still resulted in a 12% loss in resliced activity concentrations when the images were reoriented through an angle of 45° .

Reorientation Angle. This study also showed the dependence of the reorientation errors on the angle through which the images are rotated. The angle of reorientation can be minimized by employing a tiltable gantry on the PET device. A gantry offset angle of 20° may cause the reorientation angle to decrease from 45° to 25° , thus providing a substantial decrease in the amount of lost activity in the reoriented images (Table 1).

The Type of Interpolation Algorithm. Senda et al. (1)

used a three-dimensional linear interpolation algorithm (also referred to as "trilinear" interpolation) for reorientation, while Hicks et al. (7) employed two two-dimensional linear (or "bilinear") interpolation passes through the data volume. The latter method is more appropriate for reorienting SPECT images, because the denser axial sampling of SPECT relative to PET allows the cruder but faster two-dimensional linear interpolation to be substituted for the more accurate but slower three-dimensional linear interpolation. Senda's (1,6) reoriented cardiac PET images contain visual artifacts, while Hicks et al. (7) reported errors in tissue radionuclide concentrations obtained from reoriented cardiac PET images.

Two types of interpolation algorithms were investigated here. One was the conventional three-dimensional linear interpolation and the other a hybrid, consisting of two-dimensional linear interpolation together with one-dimensional cubic convolution interpolation. With respect to activity loss and spatial distortion, the hybrid interpolation algorithm consistently outperformed the linear interpolator. At a reorientation angle of 45°, hybrid interpolation resulted in a 12.5% error and in a 15% error for linear interpolation. This is approximately a 20% difference in error between the two interpolators.

In conclusion, quantitation of reoriented cardiac PET images is feasible if: (a) the data have been acquired in a prudent manner, (b) the reorientation is carried out with an effective three-dimensional interpolation algorithm and (c) any inhomogeneities in spatial resolution in the reoriented images are accounted. We recommend gantry tilting on all patients and the use of the hybrid interpolation algorithm for reorientating images. Interpolating scans are not recommended if the scanner has an axial sampling of 7 mm/plane or less. It may be possible to correct for count loss and image distortion by using the data in Tables 1 and 2 in calibration curves. For example, if the angle of reorientation is 45°, it would be possible to boost the activity in each ROI by 12.5% and decrease estimated wall thicknesses by 5% (noninterleaved case). Further studies, however, would be necessary to validate the efficacy of such corrective measures.

APPENDIX

The three-dimensional PSF can be modeled as Gaussian in all directions. Therefore:

$$\text{PSF} = \exp(-x^2/2\sigma_x^2 - y^2/2\sigma_y^2 - z^2/2\sigma_z^2),$$

where $\sigma_x = \text{FWHM}_x/2.355$, $\sigma_y = \text{FWHM}_y/2.355$, and $\sigma_z = \text{FWHM}_z/2.355$ and (x, y, z) lie along standard scanner coordinates: x and y in the transaxial plane and z in the axial direction. Now, by simply rotating the viewing coordinate system from (x, y, z) to the new coordinates (x', y', z') , the relationship between the two systems is given by:

$$\begin{bmatrix} x \\ y \\ z \end{bmatrix} = \begin{bmatrix} \lambda_1 \lambda_2 \lambda_3 \\ \mu_1 \mu_2 \mu_3 \\ \vartheta_1 \vartheta_2 \vartheta_3 \end{bmatrix} \begin{bmatrix} x' \\ y' \\ z' \end{bmatrix}, \quad \text{Eq. A1}$$

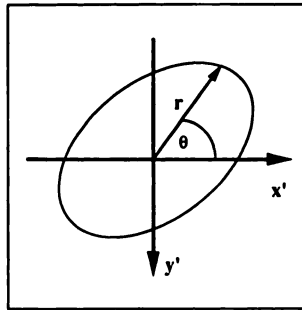


FIGURE A1. Ellipse of intersection obtained from the intersection of the reslice plane with an isocontour of the tomograph's PSF.

where the x' -axis, y' -axis and z' -axis have direction cosines $(\lambda_1, \mu_1, \vartheta_1)$, $(\lambda_2, \mu_2, \vartheta_2)$, and $(\lambda_3, \mu_3, \vartheta_3)$, respectively, with respect to the old system of axes.

The equation of a convenient ellipsoid which is an isocontour of the PSF at $1/e$ of its peak is now given by:

$$1 = x^2/2\sigma_x^2 + y^2/2\sigma_y^2 + z^2/2\sigma_z^2. \quad \text{Eq. A2}$$

Substituting Equation A1 into Equation A2 and setting z' to zero obtains the equation of the ellipse, which results from the intersection of the $(x', y', 0)$ reslice plane with the ellipsoid:

$$1 = (\lambda_1 x' + \lambda_2 y')^2/2\sigma_x^2 + (\mu_1 x' + \mu_2 y')^2/2\sigma_y^2 + (\vartheta_1 x' + \vartheta_2 y')^2/2\sigma_z^2. \quad \text{Eq. A3}$$

If this equation is plotted in the x', y' plane, this elliptical intersection would appear as illustrated in Figure A1.

By making the substitution $x' = r \cos \theta$ and $y' = r \sin \theta$ into Equation A3 gives:

$$1 = r^2[(\lambda_1 \cos \theta + \lambda_2 \sin \theta)^2/2\sigma_x^2 + (\mu_1 \cos \theta + \mu_2 \sin \theta)^2/2\sigma_y^2 + (\vartheta_1 \cos \theta + \vartheta_2 \sin \theta)^2/2\sigma_z^2]. \quad \text{Eq. A4}$$

Equation A4 may be solved for r^2 as a function of θ . In addition, since $1 = r^2/2\sigma_{\text{eff},\theta}^2$ then $r^2 = 2\sigma_{\text{eff},\theta}^2$, where $\sigma_{\text{eff},\theta}$ is the effective spatial resolution of the image in the direction of θ . The effective FWHM in the reoriented image can then be found at the angle θ :

$$\text{FWHM}_{\text{eff},\theta} = 2.355 \sigma_{\text{eff},\theta} = 2.355 r/\sqrt{2}. \quad \text{Eq. A5}$$

ACKNOWLEDGMENTS

Operated for the U.S. Department of Energy by the University of California under Contract #DE-FC03-87ER60615. This work was supported in part by the Director of the Office of Energy Research, Office of Health and Environmental Research, Washington, DC, by research grants #HL 29845 and #HL 33177, National Institutes of Health, Bethesda, MD and by an Investigative Group Award by the Greater Los Angeles Affiliate of the American Heart Association, Los Angeles, CA. William Kuhle is the recipient of an American Heart Association Medical Student Research Fellowship. Presented in part at the 37th Annual Meeting of the Society of Nuclear Medicine, Washington, DC, June 1990.

REFERENCES

1. Senda M, Yonekura Y, Tamaki N, et al. Interpolating scan and oblique-angle tomograms in myocardial PET using nitrogen-13-ammonia. *J Nucl*

- Med* 1986;27:1830-1836.
- Garcia E, Van Train K, Maddahi J, et al. Quantification of rotational thallium-201 myocardial tomography. *J Nucl Med* 1985;26:17-26.
 - O'Brien A, Gemmell H. Effectiveness of oblique section display in thallium-201 myocardial tomography. *Nucl Med Comm* 1986;7:609-616.
 - DePasquale E, Nody A, DePuey E, et al. Quantitative rotational TI-201 tomography for identifying and localizing coronary artery disease. *Circulation* 1988;77:316-327.
 - Tamaki N, Yonekura Y, Mukai T, et al. Segmental analysis of stress thallium myocardial emission tomography for localization of coronary artery disease. *Eur J Nucl Med* 1984;9:99-105.
 - Senda M, Yonekura Y, Tamaki N, et al. Axial resolution and the value of the interpolating scan in multislice positron computed tomography. *IEEE Trans Med Imaging* 1985;4:44-51.
 - Hicks K, Ganti G, Mullani N, Gould KL. Automated quantitation of three-dimensional cardiac positron emission tomography for routine clinical use. *J Nucl Med* 1989;30:1787-1797.
 - Raylman R, Hutchins G, Schwaiger M, Paradise A. Axial sampling requirements for 3-dimensional quantification of myocardial function with positron emission tomography. *IEEE Trans Nucl Sci* 1989;36:1030-1033.
 - Schafer RW, Rabiner LW. A digital signal processing approach to interpolation. *Proc IEEE* 1973;61:692-702.
 - Carter WH. Image sampling and interpolation. *SPIE* 1983;397:477-486.
 - Keys RG. Cubic convolution interpolation for digital image processing. *IEEE Trans Acoust, Speech, Signal Processing* 1981;ASSP-29:1153-1160.
 - Maeland E. On the comparison of interpolation methods. *IEEE Trans Med Imaging* 1988;7:213-217.
 - Gambhir S. Quantitation of the physical factors affecting the tracer kinetic modeling of cardiac positron emission tomography data. PhD dissertation. University of California, Los Angeles 1990.
 - Bard Y. *Nonlinear parameter estimation*, 1st edition. New York: Academic Press; 1974:341.
 - Karp J, Muehllehner G, Mankoff D, et al. Tomograph with volume imaging capability. *J Nucl Med* 1990;31:617-627.
 - Mullani N, Gould K, Hartz R, et al. Design and performance of posicam 6.5 BGO positron camera. *J Nucl Med* 1990;31:610-616.

(continued on page 1215)

SELF-STUDY TEST ANSWERS

This concept is consistent with the "mean marrow dose," which incorporates a linear dose-response model (500 rads to 50% the marrow would have the same effect as 250 rads to 100% of the marrow). Such an approach is clearly inconsistent with a dose model that incorporates terms that are quadratic or otherwise nonlinear (the model assumes that 50 rads to 10% of an organ is equivalent to 5 rads to the whole organ—a linear extrapolation). Furthermore, if partial-body doses are high enough to kill a significant number of cells, the hypothesis is surely invalid.

The dose-equivalent concept is not related to partial organ irradiation, but provides a method of expressing all kinds of radiation exposures on a common scale for calculating the effective absorbed dose.

References

- International Commission on Radiological Protection. *Radiosensitivity and Spatial Distribution of Dose*. Publication 14. New York: Pergamon, 1969.
- Rosenstein M. *Organ Doses in Diagnostic Radiology*. U.S. Department of Health, Education, and Welfare. HEW Publication (FDA) 76-803. Washington, DC: U.S. Government Printing Office, 1976.
- Shlien B, Tucker TT, Johnson DW. The mean active marrow dose to the adult population of the United States from diagnostic radiology. *Health Phys* 1978;34:587-601.

ITEMS 33-36: Management of ^{99m}Tc Spill

ANSWERS: 33, T; 34, F; 35, F; 36, F

The amount of ^{99m}Tc spilled, 20 GBq, is slightly more than 500 mCi. This clearly is a major spill, and it cannot be ignored under any circumstances. The exposure rate constant for ^{99m}Tc is approximately 70 mR/hr/Ci at 1 m, from which it can be calculated that the exposure rate at the dose preparation area (4 m from a spill of 0.5 Ci) will be on the order of about 2 mR/hr. This is not an alarmingly high exposure rate, and work in this area can continue as necessary. However, it would most assuredly be inconsistent with ALARA philosophy to ignore the spill and to allow personnel to continue to work in the area without efforts to reduce exposure levels.

Because of the large activity of ^{99m}Tc involved and the relatively high probability of contaminating large areas of the nuclear medicine clinic and hospital if the contamination were not contained, most radiation safety officers would agree that some decontamination is necessary. The activity is not so large, however, that extraordinary precautions must be taken during the clean-up. The first step is to contain the contamination,

i.e., prevent it from spreading beyond the immediate area of the spill. The person who dropped the vial should have immediately placed enough absorbent material on the spill to soak up all of the liquid on the floor. He or she should then have called for assistance and remained in the area until a survey meter was brought to check for contamination of clothing and shoes. The second step should be stopping work long enough to plan how best to proceed. Because the radiopharmaceutical is not significantly volatile, so long as people are excluded from the contaminated area, there is no immediate hazard to anyone. The third step is to put on disposable foot covers, two pairs of disposable plastic gloves, and either a laboratory coat or a surgical scrub suit. The fourth step is to quickly remove all of the broken glass and wet absorbent material and place these into a heavy plastic bag or two nested thin plastic bags; the plastic gloves should be placed in the bag after all of the other debris has been picked up. The fifth step is to attempt to remove the remaining superficial contamination on the walls, cabinets, and floor. All of these contaminated materials should be removed from the clinic area and placed in an approved radioactive waste storage area over the weekend for decay. The dose rate in the area of the spill, which now will be substantially lower than initially, should be reassessed with a survey meter. At this point most radiation safety officers probably would recommend labeling the area with the proper radioactive materials caution signs, cautioning nuclear medicine personnel to avoid the area of the spill for the remainder of the day and over the weekend, and allowing the ^{99m}Tc to decay over the weekend. The contaminated regions of the floor might also be covered with polyethylene sheeting to further reduce the likelihood of dissemination.

If the accident had occurred on Monday morning instead of Friday afternoon, the first five steps for handling the spill should be the same. In fact, this would be true regardless of the time of the week or the activity of ^{99m}Tc involved. However, because the area will be occupied more intensively during the 24-48 hr necessary for ^{99m}Tc to decay, greater attention must be paid to the dose rate from the residual contamination and to determine whether any of the residual contamination is removable and might be disseminated on individuals' shoes or clothing. The radiation safety officer should survey the laboratory and make recommendations about avoidance of the contaminated areas or other adjustments in work practices that will be required until the contamination has decayed completely.

For further in-depth information, refer to the syllabus pages in Nuclear Medicine Self-Study I.